

Toward Accurate Thermal Modeling of Phase Change Material-Based Photonic Devices

Kiumars Aryana,* Hyun Jung Kim, Cosmin-Constantin Popescu, Steven Vitale, Hyung Bin Bae, Taewoo Lee, Tian Gu, and Juejun Hu

Reconfigurable or programmable photonic devices are rapidly growing and have become an integral part of many optical systems. The ability to selectively modulate electromagnetic waves through electrical stimuli is crucial in the advancement of a variety of applications from data communication and computing devices to environmental science and space explorations. Chalcogenide-based phase-change materials (PCMs) are one of the most promising material candidates for reconfigurable photonics due to their large optical contrast between their different solid-state structural phases. Although significant efforts have been devoted to accurate simulation of PCM-based devices, in this paper, three important aspects which have often evaded prior models yet having significant impacts on the thermal and phase transition behavior of these devices are highlighted: the enthalpy of fusion, the heat capacity change upon glass transition, as well as the thermal conductivity of liquid-phase PCMs. The important topic of switching energy scaling in PCM devices, which also helps explain why the three above-mentioned effects have long been overlooked in electronic PCM memories but only become important in photonics, is further investigated. These findings offer insight to facilitate accurate modeling of PCM-based photonic devices and can inform the development of more efficient reconfigurable optics.

1. Introduction

Reconfigurable optics ranging from zoom lenses to tunable optical filters have recently garnered great interests for more compact and energy-efficient systems.^[1–5] One of the quintessential examples of the necessity for reconfigurable optics lies in the most powerful telescope ever built, The James Webb Space Telescope (JWST). At the heart of JWST, there is a near-IR (NIR) camera that enables imaging a wide variety of electromagnetic spectra from 0.6 to 5 μm . In order to selectively choose different electromagnetic wave spectra, there are 29 different passive optical filters sitting on two separate filter wheels, which are mechanically swapped depending on the operation mode.^[6–8] As amazing as this technology is, it requires bulky and complex components with mechanically moving parts that are not ideal for applications in space. Ideally, for adjusting the operation mode and imaging at different wavelengths, all 29 filters should be replaced by one unique tunable filter that can be electrically switched between different passband wavelengths with

high speed and fidelity.^[9] Light detection and ranging (LiDAR) is another technology that could benefit from nonmechanical light modulators for higher efficiency beam steering and scanning capabilities.^[10] Thus far, depending on the application, a wide variety of techniques have been proposed to modulate the electromagnetic waves using thermo-optical,^[11,12] electro-optical,^[13] magneto-optical,^[14,15] opto-mechanical,^[16] and acousto-optical effects.^[17] Nonetheless, there is still a dire need for more efficient nonmechanical tunable optics that are fast, robust, and compatible with standard semiconductor foundry fabrication processes.

One of the potential material candidates for reconfigurable optics is chalcogenide-based phase-change materials (PCMs) that undergo a solid-state phase transformation upon thermal stimuli. These materials have large optical property contrast between their amorphous and crystalline states, which makes them suitable for modulating electromagnetic waves. Another important feature of PCMs is their analog nature which enables a continuous range of properties depending on the amorphous to crystalline ratio in the material. For instance, it has been demonstrated that $\text{Ge}_2\text{Sb}_2\text{Te}_5$ (GST) can be used as a coating material to thermally camouflage objects from the background via its

K. Aryana, H. J. Kim
NASA Langley Research Center
Hampton, VA 23681, USA
E-mail: kiumars.aryana@nasa.gov

C.-C. Popescu, T. Gu, J. Hu
Department of Materials & Science Engineering
Massachusetts Institute of Technology
Cambridge, MA 02139, USA

S. Vitale
Lincoln Laboratory
Massachusetts Institute of Technology
Lexington, MA 02421, USA

H. B. Bae, T. Lee
KAIST Analysis Center
Korea Advanced Institute of Science and Technology
Yuseong-gu, Daejeon 34141, South Korea

T. Gu, J. Hu
Materials Research Laboratory
Massachusetts Institute of Technology
Cambridge, MA 02139, USA

 The ORCID identification number(s) for the author(s) of this article can be found under <https://doi.org/10.1002/sml.202304145>

DOI: 10.1002/sml.202304145

variable emissivity at different phases.^[18] More recently, PCMs have been integrated into metasurfaces in order to develop tunable properties.^[1,19–24]

To better understand the operation of these devices and rationally guide their design, considerable efforts have been dedicated to precise modeling of PCMs' phase transition behavior.^[25,26] However, to date, the vast majority of the investigations have focused on electronic memory configurations, which do not apply to photonic devices where electrothermal switching via external micro-heaters rather than direct current injection is employed.^[27]

In addition, for the application of PCMs in functional photonic devices, it is preferred to switch a larger volume of PCM to increase its overlap with the optical mode, thereby maximizing the optical contrast.^[28,29] While this is less of a concern for memory applications where the volume of phase change units are on the order of a few nanometers,^[30,31] achieving reversible switching of PCM at large length scales on the order of microns or greater presents several challenges in comparison to conventional nanoscale memory cells. These challenges include slower heat dissipation, greater atomic migration, higher power consumption, and potential delamination, all of which can negatively impact the uniformity and durability of the phase transition.^[32,33] Therefore, thermal management plays a critical role in improving the performance of PCM-based devices, especially as their length scales increase.

Furthermore, while several studies have explored thermal and kinetic modeling of the PCM crystallization process,^[34–38] the amorphization transition has received much less attention. We argue that the ability to accurately characterize the amorphization process is equally—if not more—important. Amorphization involves raising the PCM above its melting point (>600 °C) followed by rapid cooling ($\approx 10^8$ – 10^{11} K s⁻¹),^[39–41] which is a far more thermally vigorous process than crystallization. Therefore, the reliability and endurance of PCM devices are largely impacted by amorphization.^[42] It has also been shown that the amorphization process can influence the crystallization speed in the subsequent cycle,^[43–45] and thus, it plays a consequential role in the repeatability of the switching process, especially during multi-level operation.^[46,47]

In this paper, we examined the impact of three previously largely overlooked effects—the enthalpy of fusion, temperature-dependent heat capacity, as well as the thermal conductivity of liquid-phase PCMs—on its phase transformation. The results presented here show a good agreement with experimental observation and would enable accurate modeling of PCM devices while providing insight into the development of large-scale, robust, and energy-efficient PCM-based devices.

2. Device Configuration and Thermal Modeling

In our models, we have adopted a doped Si micro-heater design similar to that reported by Rios et al.^[48] **Figure 1a** illustrates 3D schematic of the heater device configuration and the layer structures. The top-view image of the fabricated device is presented in **Figure 1b,c** using two imaging techniques, scanning electron microscopy (SEM) and NIR camera. In this configuration, the PCM pixel covers around 50% of the underneath Si heater area, with lateral sizes of 140 and 200 μm, respectively. We choose Si heaters because they are transparent in both the NIR

and mid-infrared (MIR) regimes and have shown to have reliable stability.^[47–49] This enables operation in the transmissive mode instead of reflective, a critical factor in the development of reconfigurable optics such as meta-lenses, filters, and beam steering. Moreover, Si heaters are also compatible with standard foundry manufacturing^[50] to facilitate scalable deployment of PCM-based devices. In order to switch PCM between amorphous and crystalline phases, we use a function generator and a power supply to deliver the high current necessary to heat up the Si heater to sufficiently high temperatures. The resistance of the devices varies in the range of 40–50 Ω due to fabrication inhomogeneity, which requires voltages from 36 to 46 V for amorphization depending on the device resistance. The conclusions drawn from our study are equally applicable to other electrothermal PCM switching configurations as well.

In order to examine the thermal transport and temperature distribution within the proposed device architecture, we utilized finite element simulation software (COMSOL Multiphysics). A 2D model of the device was created based on its dimensions, which were established through scanning transmission electron microscopy (STEM) and are illustrated in **Figure 1b,e**. The device's cross section schematic was used as the basis for the model, as shown in **Figure 1d**. Our primary focus in this study is investigating the amorphization process, therefore, we assume that the initial state of the PCM is fully crystalline, unless stated otherwise. The simulations were performed at room temperature, with constant temperature set to 24 °C at the boundaries of the simulation domain far away from the device (**Figure 1g**). To ensure accurate modeling, we selected a domain size ten times larger than the device width, and we validated this assumption by extending the matrix lengths ranging from 10 to 50 times larger sizes, finding no impact on the device's temperature distribution. Given the microscale dimensions and fast thermal transport timescale in addition to the exceptionally low thermal conductivity of air compared to other materials within the device, it is a reasonable assumption to disregard convection and radiation effects and set the top surface as an insulative boundary condition. Further, we assumed a constant thermal boundary conductance of 100 MW m⁻² K⁻¹ across all interfaces to capture interfacial thermal resistance between different materials.^[32] The thermal conductivity of the PCM layer, denoted as $\kappa(T)$, was assumed to vary with temperature based on ref. [53], while the remaining material properties for the simulated non-PCM layers were considered to be temperature-independent as presented in **Table 1**.

In our investigation of the amorphization process, we take Ge₂Sb₂Se₄Te (GSST) which is a widely used PCM for optical applications due to its low loss absorption in the infrared regime.^[56,57] We presume that once the temperature of the PCM surpasses the melting point 600 °C, the liquid part completely transitions into the amorphous phase once cooled down. The simulation results depicted in **Figure 1h** show the progression of the amorphized region in relation to the base crystalline state upon thermal excitation. It is important to note that the contour plots are not drawn to scale, as the width of the PCM is 750 times greater than its thickness.

In order to experimentally illustrate the amorphization process, we deposited 140 μm × 140 μm of GSST on a 200 μm × 200 μm transparent silicon heater. To prevent oxidation and improve heat dissipation during the amorphization process, we

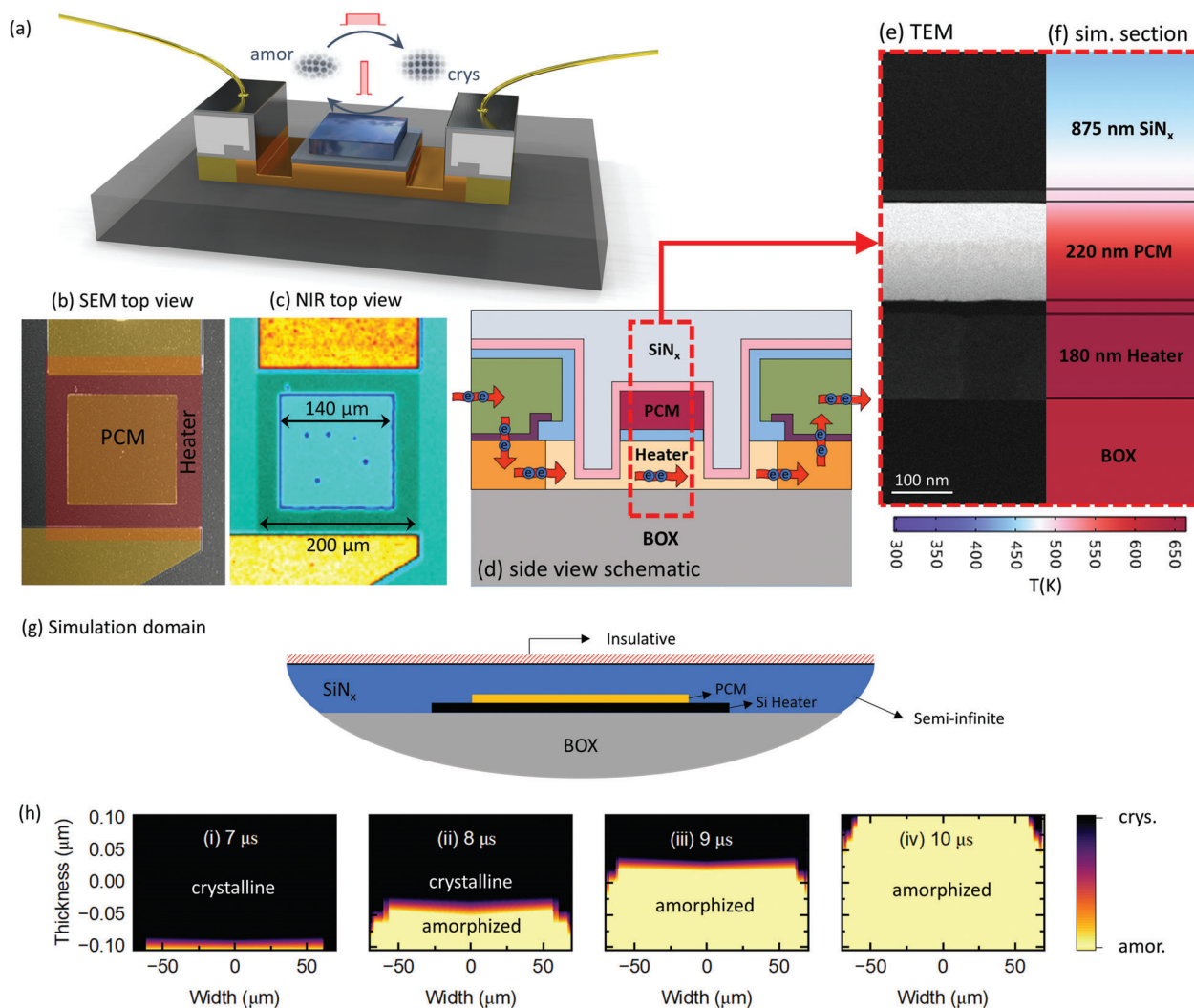


Figure 1. This figure illustrates the configuration of PCM-based device studied in this paper. Panel (a) provides a 3D schematic of the device configuration, while panels (b) and (c) show top view images obtained using scanning electron microscopy (SEM) and near-infrared (NIR) camera (FLIR A6262) with a wavelength range of 600–1700 nm. Panels (d–f) depict cross-sectional view of the device with all the layers adjacent to the PCM, accompanied by corresponding transmission electron microscopy (TEM) image and simulation sections that are the focus of this study. The simulation domain, along with the relevant boundary conditions used in this study, are presented in panel (g). Panel (h) shows the expansion of the amorphous region within the crystalline state due to thermal excitation from the heater underneath. The time stamp denotes the duration since the initiation of the heating pulse. Note that the images are not drawn to scale.

encapsulated the device with 875 nm sputtered SiN_x . While the device configuration utilized in this study is primarily intended for transmission measurements, it is important to note

Table 1. Room temperature properties of materials used in the simulations.

Film	Thickness [nm]	Thermal Conductivity [$\text{W m}^{-1} \text{K}^{-1}$]	Specific Heat [$\text{J kg}^{-1} \text{K}^{-1}$]	Density [kg m^{-3}]
SiN_x	875	2.0 ^[51]	1631	3100
Al_2O_3	25	2.0 ^[52]	880	3950
GSST	210	$\kappa(T)$ ^[53]	240 ^[53,54]	6200
SiO_2	30	1.35 ^[55]	1000	2650
Si heater	180	135 ^[55]	710	2329

that for the purpose of this particular investigation, which is focused on illustrating the growth of the amorphized region, we are solely examining the reflectivity of the surface. Using a NIR camera (FLIR A6262), which operates in 600–1700 nm wavelength range, we monitored changes in the PCM's reflectivity as we sent successive amorphization pulses. The GSST is initially in the crystalline phase. Upon sending incremental amorphization pulses that are separated by 30 s, we ensured the device reached equilibrium at room temperature before each image was collected.

Figure 2 shows the incremental pulses applied to the PCM and the percent change in the reflectivity of the surface with respect to the applied voltage. As can be seen in the images presented in Figure 2c, the sample did not show any change for pulses with amplitudes up to 42 V. As soon as the voltage

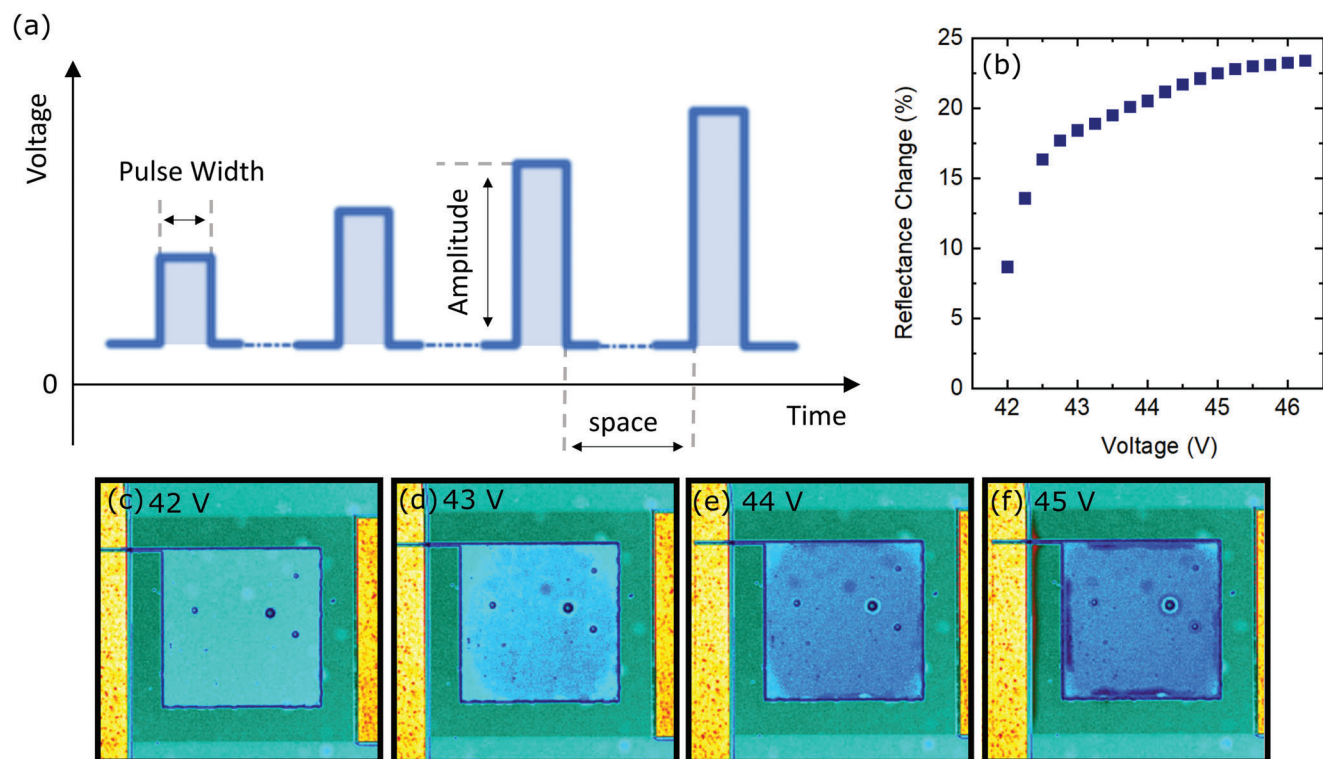


Figure 2. a) Incremental sequential pulses that are applied to GSST on a heater with 10 μ s pulse width and 30 s interval period. b) Changes in the reflectivity of the GSST with respect to base crystalline phase as a function of applied voltage. c–f) Images from the surface of the GSST upon application of different voltages and progression of the amorphous phase.

exceeded this threshold, the reflectivity of the center of the sample began to decrease which is indicative of partial amorphization. On the other hand, at the boundaries of PCM and near the corners (Figure 2d) we observed no change in the color of PCM, which we believe is due to nonuniform temperature distribution across the PCM. This is consistent with our simulated temperature distribution in the PCM for low amplitude pulses that lead to partial amorphization, consistent with the results presented in Figure 1h. Upon increasing the pulse voltage, the change in the color became more pronounced and the unswitched crystalline regions closer to the edges began to amorphize. From these results, we can see the reflectivity plateaus at 45.5 V, where upon increasing the voltage no observable change in the reflectivity of the PCM was detected. The recorded resistance of the device studied here stands around 40 Ω . Taking the resistance and applied voltage into account, the peak power for the amorphization pulse can be calculated to be approximately 52 W. In practical terms, given that the amorphization pulse lasts for only 10 μ s, the energy necessary for amorphization amounts to 520 μ J. In the subsequent sections of the manuscript, we will present the peak power corresponding to the amorphization pulse. By approximating the changes in the reflectivity of the PCM with respect to its initial crystalline phase, we observed an \approx 23% change in the reflectivity upon complete transformation to the amorphous state. In the following section, we will elaborate on several important factors that should be properly considered to enable accurate modeling of the progressive amorphization process shown here.

3. Enthalpy of Fusion and Heat Capacity of Supercooled Liquids

In this section, our focus is on examining the impact of enthalpy and heat capacity on the phase transformation of PCMs, namely GST and GSST. As experimental data for the enthalpy of GSST is unavailable, we utilize the values from GST and apply them to both cases. **Figure 3a** plots the classical enthalpy–temperature curves of a glass-forming solid. ΔH_c and ΔH_f denote the enthalpies of crystallization and fusion in GST, respectively. The former gives the enthalpy difference between a solid’s amorphous and crystalline states, whereas the latter, also known as the latent heat of melting, represents the energy required to change the state of a crystalline solid unit mass to liquid at the melting point, without a temperature increase. The other important feature evidenced by this figure is that while the heat capacity of the crystal solid (represented by the slope of the curve) is relatively insensitive to temperature up to its melting point, the heat capacity of the amorphous phase increases considerably from the glassy state near room temperature to the supercooled liquid state past glass transition. This is attributed to the increasing degrees of freedom that the atoms can access in the liquid phase versus in the solid phase.^[58]

The significance of the enthalpy–temperature relation in the PCM switching process is twofold. First, during amorphization, additional heat must be supplied to convert the solid phase into liquid and during the process, the temperature at the solid–liquid interface is held constant. This effect, even though not accounted

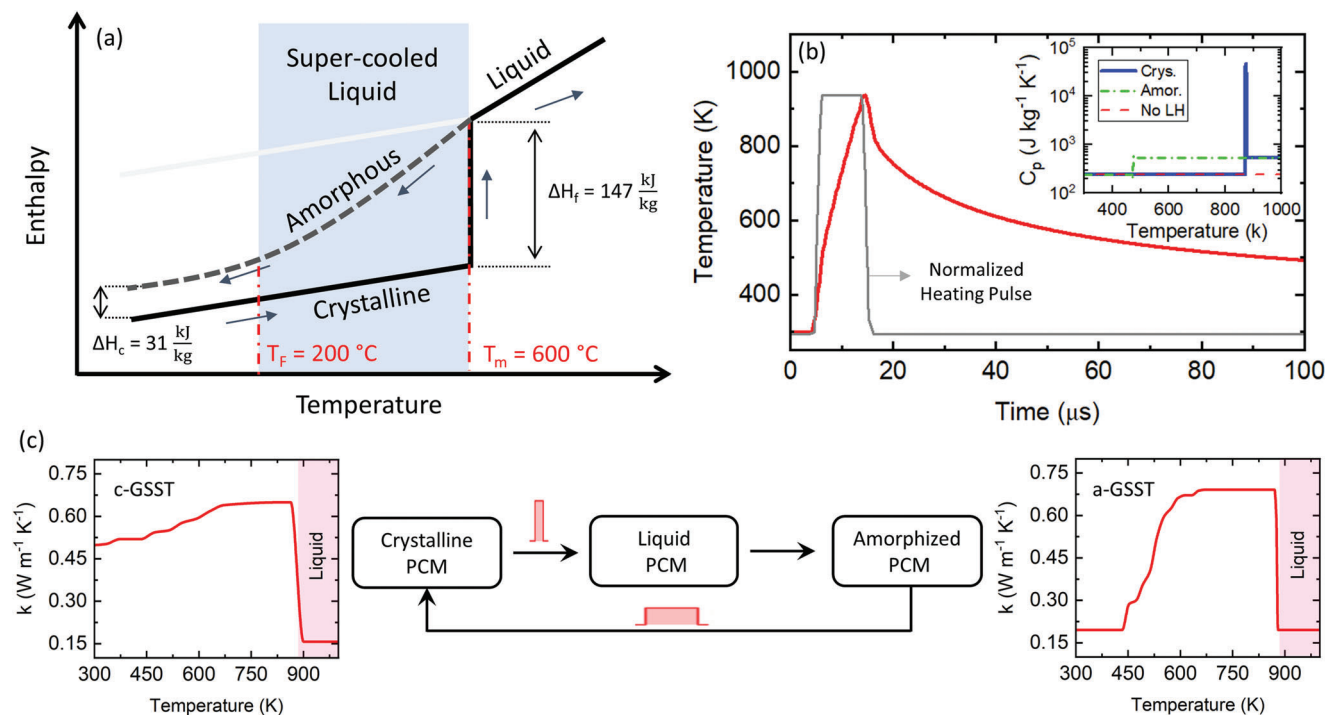


Figure 3. a) The enthalpy–temperature curves for GST, showing classical patterns observed during solid–liquid phase transition as well as glass transition, and b) maximum temperature profile and pulse shape within the PCM during the amorphization cycle. The inset shows heat capacity trend as a function of temperature for crystalline and amorphous phases, as well as when latent heat (LH) of melting is not considered. c) The switching cycle and the corresponding thermal conductivity trend as a function of temperature for the amorphous and crystalline phase of GSST. The thermal conductivity data below the melting point are sourced from ref. [53], while for temperatures above the melting point, we have made informed speculation.

for in some prior studies,^[59,60] can significantly alter the temperature distribution and solid–liquid interface location. For PCMs, the ΔH_f ranges from 98 to 147 kJ kg^{-1} ,^[54,61–63] and the corresponding latent heat is equivalent to the energy needed to raise the temperatures by nearly 600 K. Therefore, the enthalpy of fusion is an important factor in thermal modeling, especially when the PCM device size is large, as we will explain later.

The second implication is more subtle and to our knowledge has not been explicitly discussed in literature. In previous thermal simulations of PCM-based photonic devices,^[64–71] the heat capacity of amorphous PCM has been quoted as a constant up to the melting point. However, as can be seen from Figure 3a, the heat capacity of amorphous PCM is not constant and must increase when transitioning into the supercooled liquid state, or when heated to above its fictive temperature. Assuming a constant heat capacity will underestimate the amount of energy needed to bring the amorphous PCM to the melting point, roughly by $\Delta H_f - \Delta H_c$. In PCMs, ΔH_c ranges between 31 and 65 kJ kg^{-1} .^[54,72–75] For GST, $\Delta H_f - \Delta H_c = 116 \text{ kJ kg}^{-1}$. The temperature-dependent heat capacity can therefore significantly impact thermal simulation results in PCM devices, as we will show later.

In order to demonstrate the impact of enthalpy of fusion on the phase transformation during the amorphization process, we consider two cases: one where latent heat of melting is taken into account ($\Delta H_f = 147 \text{ kJ kg}^{-1}$), which appears as a spike in heat capacity between 870 and 876 K as shown in the inset in Figure 3b, and one where it is (erroneously) not considered (ΔH_f

$= 0$). Figure 3c illustrates the switching cycles in PCM-based devices that undergo a liquid phase during amorphization, as well as the corresponding thermal conductivity trend as a function of temperature for both the crystalline and amorphous phases.

Figure 4a,b shows the different modeling outcomes of the amorphization cycle in the GSST device in the two cases mentioned above. The contour plots provide a comparison of the percentage of amorphized volume and temperature distribution for GSST when considering the latent heat versus ignoring it. When considering the effect of latent heat, Figure 4a,b illustrates that at the same input power, a smaller PCM volume undergoes solid–liquid phase transformation. This is because some of the energy in the crystalline phase is utilized to overcome the latent heat of melting, resulting in a lower temperature increase, less molten GSST, and consequently, less amorphization. Figure 4a,b demonstrates that neglecting the impact of latent heat would result in a nearly 18% overestimation of the amorphized area and temperature distribution in the PCM for an input peak power of 26 W.

Next, we examine the influence of the temperature-dependent heat capacity of PCMs. Unfortunately, experimental data on the heat capacity of the (supercooled) liquid phase of PCMs are not available, and therefore, we will need to make some educated assumptions. We start by assuming that the heat capacity as a function of temperature remains the same up to the fictive temperature T_F , beyond which the heat capacity abruptly increases to the (supercooled) liquid phase value. This is a valid approximation as glass transition typically occurs over a narrow temperature window compared to the entire amorphization process. We further

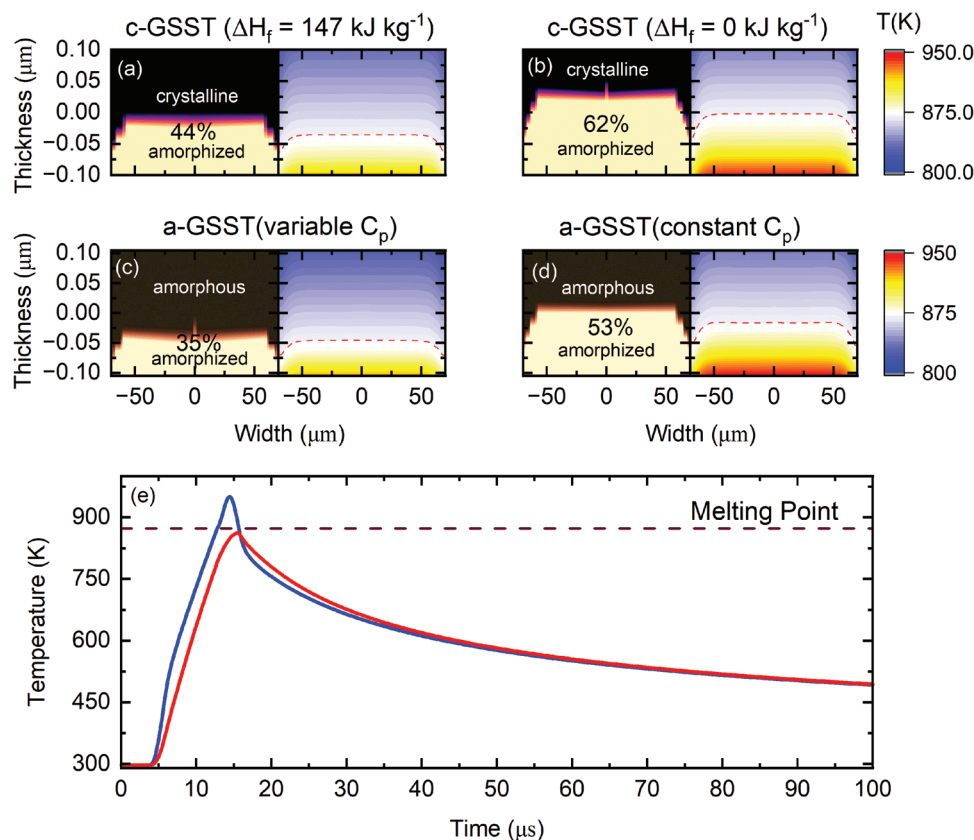


Figure 4. This figure illustrates the phase transformation and temperature distribution in PCM for GSST after amorphization pulse under various conditions, including: a) considering the enthalpy of fusion ($\Delta H_f = 147 \text{ kJ kg}^{-1}$), b) disregarding the enthalpy of fusion ($\Delta H_f = 0 \text{ kJ kg}^{-1}$), c) variable heat capacity, and d) constant heat capacity as a function of temperature. The contour plots are not drawn to scale, as the width of the PCM is 750 times greater than its thickness. The melting temperature threshold is denoted by the dashed red line in the 2D temperature contour. e) The maximum (blue) and minimum (red) temperatures rise within PCM volume with respect to time.

assume a fictive temperature of $T_F = 200 \text{ }^\circ\text{C}$, which corresponds to the approximate temperature range of glass transition measured in GST. If we further quote the $\Delta H_f = 147 \text{ kJ kg}^{-1}$ and $\Delta H_c = 31 \text{ kJ kg}^{-1}$ values from GST, then the heat capacity jump at T_F can be obtained from $\Delta C_p = (\Delta H_f - \Delta H_c)/(T_m - T_F)$, where T_m represents the melting point. Following this, we take a constant heat capacity of 240 and $528 \text{ J kg}^{-1} \text{ K}^{-1}$ for below and above T_F , respectively. In this case, since we are studying the melting of an amorphous phase, we assume that the amorphization pulse is sent to an already amorphous PCM. This may seem redundant, but it provides critical insights for investigating the thermal properties of the amorphous phase in multi-level programming, where a mixture of amorphous and crystalline phases is present. As shown in Figure 4c,d, assuming a constant heat capacity as a function of temperature, similar to the crystalline phase, overpredicts the amorphization and temperature rise in the PCM. Figure 4e shows the temperature rise as a function of time during crystalline-to-amorphous phase transition for location points in the GSST; center and closest to the heater (blue line), and center farthest from the heater (red line). According to this plot, the temperature gradient along the thickness of the GSST can reach as high as $\approx 104 \text{ K}$ at the peak temperature. This large temperature gradient could lead to nonuniformity and reduced lifetime. Further, it is important to note that, in all cases, when the based

phase is crystalline (Figure 4a,b), a higher amorphization rate is achieved compared to the cases where the base phase is amorphous (Figure 4c,d). The subsequent section will discuss the importance of the thermal conductivity of PCM during the amorphization process.

4. Thermal Conductivity of Liquid Phase

From the previous section, we observed that thermal conductivity of the PCM plays an important role in the degree of amorphization. For developing reliable devices with an extended lifetime, a uniform temperature distribution across the PCM during the amorphization cycle is a necessity. Theoretically, for triggering amorphization of the PCM, we need to deliver enough power to uniformly raise its temperature a few degrees above the melting point. Nonetheless, considering most PCMs have typically low thermal conductivity ($< 1 \text{ W m}^{-1} \text{ K}^{-1}$), as the device length scale increases, the formation of a nonuniform temperature profile is inevitable. Using the right combination of materials and device design, we can mitigate this nonuniformity and potentially help improving the device durability. For the PCM with embedded heater configuration, which is the focus of this study, we demonstrated that the center of the device at the interface between the PCM and heater reaches the highest

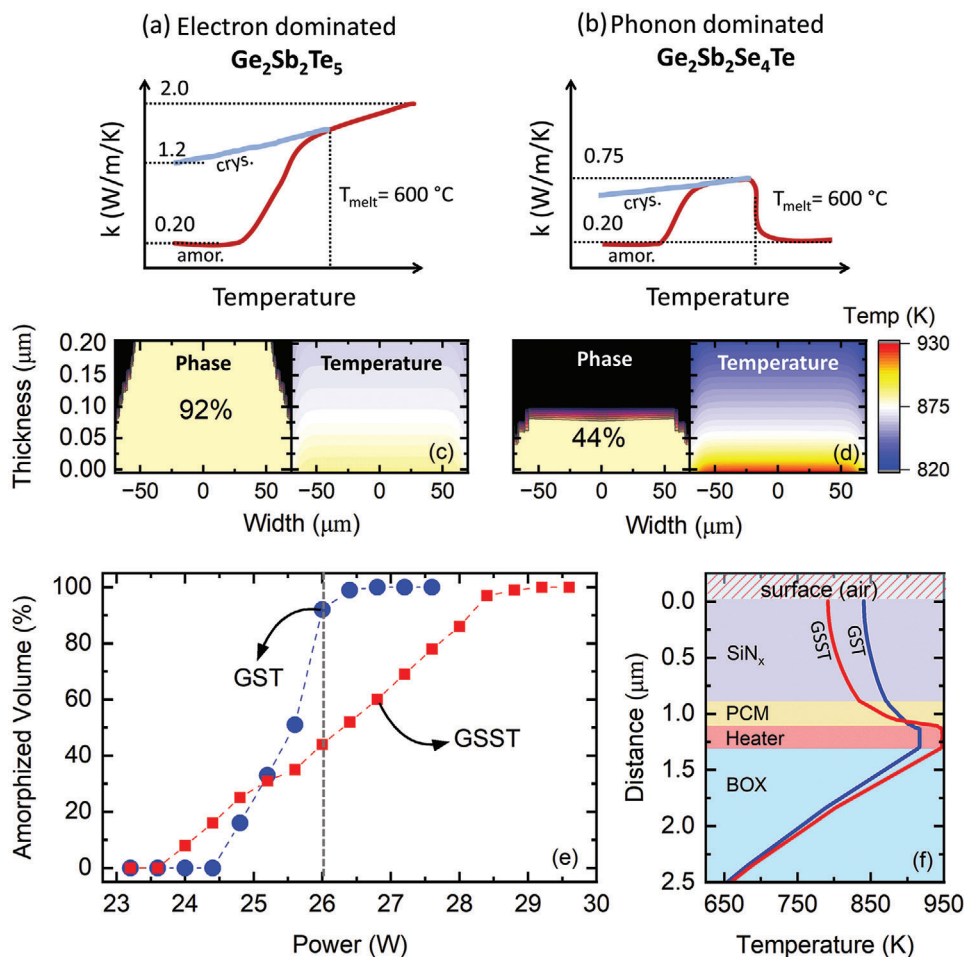


Figure 5. a,b) Qualitative thermal conductivity trend for GST and GSST with respect to temperature. The actual values for temperature-dependant thermal conductivity that are used in the simulations can be found in ref. [53]. c,d) PCM thermal conductivity effect on the phase transformation and temperature distribution. e) Percentage of amorphized PCM at different input power for GST and GSST. f) The through-plane temperature profile at the midpoint of the device for GSST and GST at the end of the amorphization pulse (maximum temperature rise).

temperature during the amorphization cycle leading to a flat-dome-shaped amorphized region. Thus, for increasing the amorphized volume, typically the heater must operate tens of degrees higher than the melting temperature of the PCM to amorphize regions away from the heater. This, however, could be a major issue as a higher temperature would create a localized hot spot and impose a larger thermal strain on the device. In this section, we discuss the importance of PCM intrinsic thermal conductivity for a more uniform temperature distribution and greater degree of phase transformation.

Although most PCMs have intrinsically low thermal conductivity, depending on their compositions, they behave significantly differently at high temperatures, especially in the liquid phase. For instance, it has been shown that the thermal conductivity of fully crystalline GST is driven by electrons, whereas in fully crystalline GSST, the electronic contribution is significantly suppressed and the thermal transport is driven by phonons.^[53] This means that the GST thermal conductivity increases with temperature as depicted in **Figure 5a** even in the liquid phase due to the increased contribution of electronic carriers which is also

consistent with prior electrical conductivity measurements in its liquid phase.^[76–79] On the other hand, upon solid–liquid phase transformation, the thermal conductivity of GSST is expected to drop to its amorphous value due to disruption of periodicity and emergence of disorder in the atomic structure (see **Figure 5b**). It is noted that there are no reports for the thermal conductivity of GSST in the liquid phase to validate or refute our hypothesis, yet we can make an educated speculation about how GSST behaves in its liquid phase. Considering this and using temperature-dependent thermal conductivities from ref. [53], an estimation for the amorphization percentage and temperature distribution in GST and GSST is presented in **Figure 5c,d**. The temperature contour plots show the highest temperature reached by the PCM during the amorphization cycle. Based on these results, we observe a more uniform temperature distribution in the GST layer, with a temperature gradient of only $\Delta T = 31$ K throughout the entire layer. In contrast, for the GSST case, the temperature gradient reaches $\Delta T = 104$ K. As a result of the large temperature gradient in GSST, heat transport and hence amorphization across its volume are hampered. This is evident from

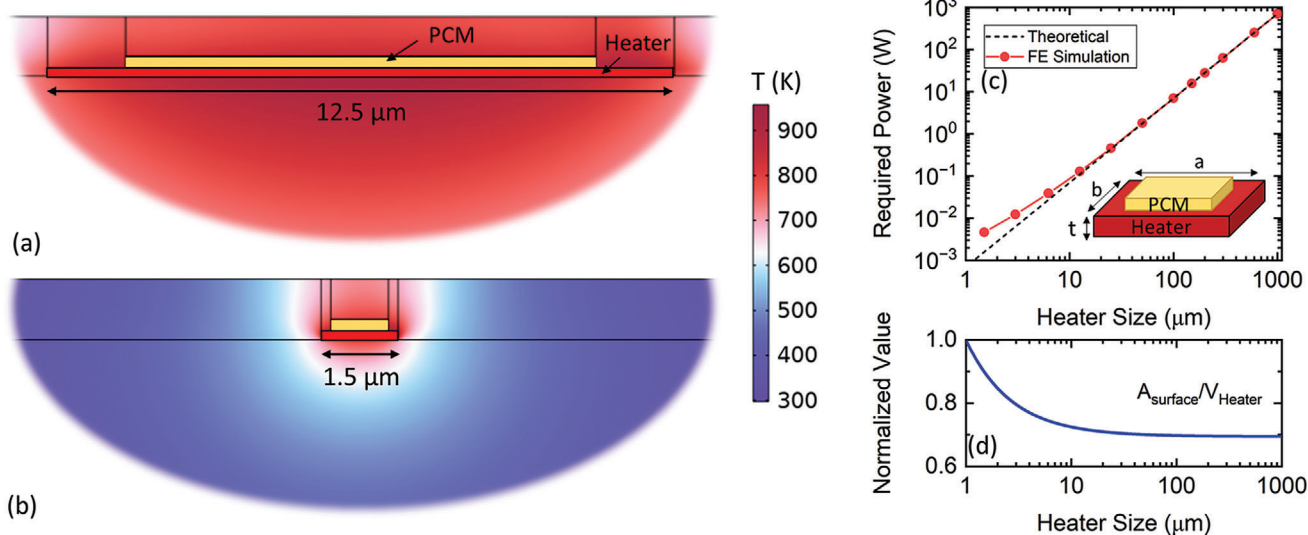


Figure 6. Temperature distribution in the PCM device with embedded heater and lateral dimension of a) 12.5 μm and b) 1.5 μm. c) The theoretical value and the simulation results for device peak pulse power with respect to the heater size from 1 to 1000 μm. d) Normalized ratio for surface area relative to volume as the lateral width of the Si heater increases from 1 to 1000 μm. In the FE simulation, the input power is adjusted to produce a similar temperature rise across all heater sizes.

Figure 5e, where the amorphization fraction in GSST consistently lags behind that in GST even for identical heater configuration and voltage pulse parameters, with an amorphization fraction difference up to 48% at peak pulse power of 26 W. Furthermore, Figure 5f displays the highest temperature reached during the amorphization pulse (after 10 μs) for GSST and GST across various layers in the stack. As per the plot, the maximum temperature recorded for the GST case is 916 K, whereas for GSST, it is 947 K. Thus, if GST is employed as the PCM under identical conditions, the Si heater temperature would remain 31 K lower than in the case of GSST. This marked difference highlights the critical importance of quantifying liquid-phase thermal conductivity to allow for material-specific thermal management and reliable PCM switching in photonic devices.

5. Switching Energy and Size Scaling in PCM-Based Devices

This section aims to examine the effect of scaling PCM-based devices on their energy consumption and overall performance. According to Fourier's law, the energy required to heat a material is proportional to its cross-sectional area (A), with $Q = -kA(dT/dx)$, assuming a constant thermal conductivity (k) and temperature gradient (dT). Thus, doubling the area of a material results in doubling of the energy required to generate the same temperature gradient. Nonetheless, in a device configuration, it is not only the PCM that heats up during the switching cycles but also the surrounding materials. The rate of heat loss from PCM to the surrounding materials depends on its surface area, which increases less rapidly than the volume as the material grows in size. Consequently, smaller volumes like PCM-based memory cells in storage devices have a larger surface-to-volume ratio and more contact areas with the surroundings, resulting in a higher proportion of heat being transferred to the surroundings and more

intense thermal leakage. This means that the scaling of PCM-based devices is expected to follow a sub-linear trend. As the length scale of the PCM device increases (more quantitatively as the heater size reaches a few tens of microns), the switching energy is increasingly being dominated by the intrinsic properties of the PCM rather than those of surrounding materials. It therefore comes as no surprise that the aforementioned effects resulting from enthalpy of fusion, supercooled liquid heat capacity, and liquid phase thermal conductivity have long been neglected in electronic memories and only become relevant in photonic devices. In order to investigate this, we use our finite element model and change the lateral dimension of the heater and PCM in order to assess the impact of size on the power consumption.

Figure 6a,b depicts the temperature distribution during the amorphization pulse for two different device sizes. In this particular device architecture, the power consumption is determined by the heater size. To perform the simulations, the device size, or more accurately, the heater size, is varied from 1.5 μm × 1.5 μm, where the thickness of the PCM (≈ 210 nm) is comparable to the device lateral dimension, to 1000 μm × 1000 μm, where the thickness of PCM is negligible compared to the heater lateral dimension. To enable a meaningful comparison of power consumption among devices with varying heater sizes, we select a 200 μm heater as a benchmark. For this, an input peak pulse power of 28 W is required to attain 86% amorphization and a maximum temperature rise of around 1000 K when subjected to a 10 μs pulse. Upon changing the device size, we adjust the input power to get the same level of amorphization (86%) and temperature rise (1000 ± 5 K) across all heater sizes. Theoretically, since heat (Q) and effective area (A) have a linear relation, as the areal size of the heater decreases, we would expect a linear reduction in the power consumption, where for a heater with a smaller size of 1.5 μm, 1.5 mW of power is expected to generate the same temperature rise as in the 200 μm heater. This is shown as the

dashed line in Figure 6c, where the inset shows the configuration of the PCM on the heater indicating the area of the heater ($a \times b$) versus its thickness (t). However, simulations indicate that three times more power input (4.5 mW) is necessary for the 1.5 μm heater to generate the same temperature rise and phase transformation in the smaller heater. In other words, our simulation results for various device lateral dimensions, depicted by solid red circles, reveal that the power consumption deviates from the linear trend as the heater size decreases below 30 μm . This deviation occurs due to the fact that the surface area to volume ratio is higher for smaller devices as depicted in Figure 6d, resulting in greater thermal leakage from the boundaries to the surrounding environment. Consequently, creating the same temperature rise for the smaller heater size requires more power. This significant difference in power requirements is attributed to the larger surface area of smaller heaters relative to their volume, which leads to greater thermal leakage and, thus, a higher power demand to attain the same temperature rise. On the other hand, our results indicate that for heaters larger than 30 μm , the surface area to volume ratio remains relatively constant. Consequently, the power consumption follows a linear trend, as expected. It is important to highlight that the peak pulse power derived from simulations, 28 W, for the 200 $\mu\text{m} \times 200 \mu\text{m}$ heater size closely aligns with the measured value of 52 W. While there exists almost a twofold difference between experimental and simulated results, we view this level of agreement as satisfactory, especially considering that the simulations rely on nominal values and do not account for experimental uncertainties. In this study, the reported power magnitude corresponds to the pinnacle of power achieved during the 10 μs period of the amorphization pulse. In other words, the energy consumed during the amorphization can be calculated as the result of multiplying the pulse width by the peak power.

6. Discussion

The precise identification of influential parameters that affect temperature and phase distributions in PCM-based devices during cycling is crucial for developing more reliable devices. These simulations are especially important for validating experimental results and, more importantly, in achieving reliable multi-level operation on PCMs, which demands a more precise control over phase transformation. The results presented in this paper highlight the effective parameters in the phase transformation of PCMs and show the necessity of thermal transport consideration in developing reliable devices for future applications. The inclusion of parameters such as enthalpy of crystallization and melting, temperature-dependent heat capacity, and thermal conductivity in models can improve the agreement between simulation results and experiments. However, validating these models experimentally is challenging due to the rapid speed and microscale phase transformation of PCM-based devices. For example, neglecting a parameter such as enthalpy of melting would produce an amorphization voltage lower than experiment and hence incomplete “reset” if one was to follow the simulation result. Furthermore, the enthalpy of melting will significantly modify the temperature distribution inside PCMs, as temperature will be held constant at melting point at the solid–liquid interface.

Moreover, this study emphasizes the significance of PCMs with higher thermal conductivity, such as GST, in achieving a

more uniform temperature distribution throughout the device structure and reducing localized hotspots. This directly impacts the endurance and lifetime of the device, as the material does not need to reach temperatures significantly higher than its melting point. Consequently, unlike PCM-based memory cells that benefit from low thermal conductivity PCMs for reduced power consumption, expanding the application of PCMs to large-scale scenarios favors higher thermal conductivity PCMs to achieve a more uniform temperature distribution and prolong the device lifetime. However, it should be noted that while higher thermal conductivity PCMs offer advantages in device performance and lifespan, they may compromise optical properties. For instance, although GST has a higher thermal conductivity compared to GSST, GST exhibits higher optical absorption in the crystalline phase which could be a major issue for development of transmissive optics based on PCM.

7. Conclusion

In this study, we examined the amorphization process in large-area PCM-based photonic devices. The study specifically examined the impact of enthalpy of fusion, temperature-dependent heat capacity, thermal conductivity of liquid PCM, and scaling of device size on the phase transformation and power consumption. Our results demonstrated the importance of accounting for the enthalpy of fusion and the heat capacity change during glass transition when modeling the amorphization process. Furthermore, according to our simulations, in order to increase the dimensions of PCM-based photonic devices, PCMs with electron-dominated thermal conductivity such as $\text{Ge}_2\text{Sb}_2\text{Te}_5$ are more favorable as their thermal conductivity increases with temperature even after the solid–liquid phase transition. We compared the phase transformation degree and temperature distribution in the PCM layer for an electron-dominated PCM such as $\text{Ge}_2\text{Sb}_2\text{Te}_5$ and a phonon-dominated PCM such as $\text{Ge}_2\text{Sb}_2\text{Se}_4\text{Te}$ and showed that the electron-dominated PCM leads to less temperature rise and more uniform temperature distribution in the PCM layer while providing more than two times higher amorphization volume. Furthermore, we discovered that for devices with lateral dimensions smaller than 30 μm , the power consumption does not scale linearly with the size of the device due to the increased ratio of PCM surface area to volume. However, for devices with lateral sizes larger than 30 μm , power consumption increases linearly with device size. Overall, our findings contribute to understanding and accurate modeling of thermal transport phenomena in PCM-based photonic devices and could lead to the development of reconfigurable metasurfaces with functional properties like filters, lenses, and beam steering devices.

8. Experimental Section

STEM: The specimen for STEM observation was prepared by lift off via ion-beam technology by using a focused ion-beam (FIB) system (Helios G5 UX, ThermoFisher Scientific). Protective amorphous carbon and Pt layers were applied over the region of interest before ion milling in the FIB system. HAADF STEM images were acquired with a TEM (Titan cubed G2 60-300, ThermoFisher Scientific) at 300 kV with a spherical aberration (Cs) corrector (CEOS GmbH).

Device Fabrication: The specimen for TEM and NIR optical analysis was fabricated on a doped Si-on-insulator platform. The GSST was deposited via thermal evaporation from a pre-weighted fresh source in a custom-built deposition chamber. The film was subsequently encapsulated with 20 nm of Al_2O_3 via atomic layer deposition and further encapsulated with 875 nm of reactively sputtered silicon nitride.

Acknowledgements

This work was supported in part by the NSF Award number 2132929. The research was sponsored by the National Aeronautics and Space Administration (NASA) through a contract with ORAU. The views and conclusions contained in this document are those of the authors and should not be interpreted as representing the official policies, either expressed or implied, of the National Aeronautics and Space Administration (NASA) or the US Government. The US Government is authorized to reproduce and distribute reprints for Government purposes notwithstanding any copyright notation herein. Specific vendor and manufacturer names are explicitly mentioned only to accurately describe the test hardware. The use of vendor and manufacturer names does not imply an endorsement by the US Government nor does it imply that the specified equipment is the best available.

Conflict of Interest

The authors declare no conflict of interest.

Author Contributions

K.A., H.J.K., and J.H. designed the study. K.A. performed the simulations. C.-C.P., S.V., T.G., and J.H. fabricated the device. K.A. performed the electrical biasing measurement. H.B.B. and T.L. performed the SEM and TEM measurements. K.A. and J.H. wrote the manuscript.

Data Availability Statement

The data that support the findings of this study are available from the corresponding author upon reasonable request.

Keywords

amorphization, phase-change materials, temperature, thermal conductivity

Received: May 17, 2023
Revised: July 11, 2023
Published online: August 30, 2023

- [1] M. N. Julian, C. Williams, S. Borg, S. Bartram, H. J. Kim, *Optica* **2020**, 7, 746.
- [2] M. Y. Shalaginov, S. An, Y. Zhang, F. Yang, P. Su, V. Liberman, J. B. Chou, C. M. Roberts, M. Kang, C. Rios, Q. Du, C. Fowler, A. Agarwal, K. A. Richardson, C. Rivero-Baleine, H. Zhang, J. Hu, T. Gu, *Nat. Commun.* **2021**, 12, 1225.
- [3] K. Chaudhary, M. Tamagnone, X. Yin, C. M. Spägle, S. L. Oscurato, J. Li, C. Persch, R. Li, N. A. Rubin, L. A. Jauregui, K. Watanabe, T. Taniguchi, P. Kim, M. Wuttig, J. H. Edgar, A. Ambrosio, F. Capasso, *Nat. Commun.* **2019**, 10, 1.

- [4] H. J. Kim, S. Borg, S. Bartram, K. Aryana, W. Humphreys, J. Hu, T. Gu, S. An, Y. Zhang, C.-C. Popescu, C. Williams, M. Julian, D. Bombara, NASA Technical Reports Server **2023**.
- [5] K. Aryana, H. J. Kim, M. Julian, S. E. Borg, S. M. Bartram, W. M. Humphreys, in *Optical Components and Materials XX*, Vol. 12417, SPIE, Bellingham, WA **2023**, pp. 1241704.
- [6] J. P. Gardner, J. C. Mather, M. Clampin, R. Doyon, M. A. Greenhouse, H. B. Hammel, J. B. Hutchings, P. Jakobsen, S. J. Lilly, K. S. Long, J. I. Lunine, M. J. McCaughrean, M. Mountain, J. Nella, G. H. Rieke, M. J. Rieke, H.-W. Rix, E. P. Smith, G. Sonneborn, M. Stiavelli, *Space Sci. Rev.* **2006**, 123, 485.
- [7] C. A. Beichman, M. Rieke, D. Eisenstein, T. P. Greene, J. Krist, D. McCarthy, M. Meyer, J. Stansberry, in *Space Telescopes and Instrumentation 2012: Optical, Infrared, and Millimeter Wave*, Vol. 8442, SPIE, Bellingham, WA **2012**, pp. 973–983.
- [8] C. Beichman, B. Benneke, H. Knutson, R. Smith, P.-O. Lagage, C. Dressing, D. Latham, J. Lunine, S. Birkmann, P. Ferruit, G. Giardino, E. Kempton, S. Carey, J. Krick, P. D. Deroo, A. Mande, M. E. Ressler, A. Shporer, M. Swain, G. Vasisht, G. Ricker, J. Bouwman, I. Crossfield, T. Greene, S. Howell, J. Christiansen, D. Ciardi, M. Clampin, M. Greenhouse, A. Sozzetti, et al., *Publ. Astron. Soc. Pac.* **2014**, 126, 1134.
- [9] T. Gu, H. J. Kim, C. Rivero-Baleine, J. Hu, *Nat. Photonics* **2023**, 17, 48.
- [10] Y. Kim, J.-H. Han, D. Ahn, S. Kim, *Micromachines* **2021**, 12, 625.
- [11] N. C. Harris, Y. Ma, J. Mower, T. Baehr-Jones, D. Englund, M. Hochberg, C. Galland, *Opt. Express* **2014**, 22, 10487.
- [12] M. Bosch, M. Shcherbakov, Z. Fan, G. Shvets, *J. Appl. Phys.* **2019**, 126, 073102.
- [13] Q. Xu, B. Schmidt, S. Pradhan, M. Lipson, *Nature* **2005**, 435, 325.
- [14] L. D. Tzuang, K. Fang, P. Nussenzweig, S. Fan, M. Lipson, *Nat. Photonics* **2014**, 8, 701.
- [15] H. Takagi, K. Nakamura, T. Goto, P. Lim, M. Inoue, *Opt. Lett.* **2014**, 39, 3344.
- [16] E. Arbabi, A. Arbabi, S. M. Kamali, Y. Horie, M. Faraji-Dana, A. Faraon, *Nat. Commun.* **2018**, 9, 812.
- [17] Z. Sun, A. Martinez, F. Wang, *Nat. Photonics* **2016**, 10, 227.
- [18] Y. Qu, Q. Li, L. Cai, M. Pan, P. Ghosh, K. Du, *Light Sci. Appl.* **2018**, 7, 1.
- [19] Q. Wang, E. T. F. Rogers, B. Gholipour, C.-M. Wang, G. Yuan, J. Teng, N. I. Zheludev, *Nat. Photonics* **2016**, 10, 60.
- [20] F. Yang, H.-I. Lin, M. Y. Shalaginov, K. Stoll, S. An, C. Rivero-Baleine, M. Kang, A. Agarwal, K. Richardson, H. Zhang, J. Hu, T. Gu, *Adv. Opt. Mater.* **2022**, 10, 2200721.
- [21] M. Wang, J. S. Lee, S. Aggarwal, N. Farmakidis, Y. He, T. Cheng, H. Bhaskaran, *Adv. Sci.* **2023**, 2204899.
- [22] F. Ding, Y. Yang, S. I. Bozhevolnyi, *Adv. Opt. Mater.* **2019**, 7, 1801709.
- [23] C. R. de Galarreta, S. G.-C. Carrillo1, Y.-Y. Au, E. Gemo, L. Trimby, J. Shields, E. Humphreys, J. Faneca, L. Cai, A. Baldycheva, J. Bertolotti, C. D. Wright, *J. Opt.* **2020**, 22, 114001.
- [24] S. Abdollahramezani, O. Hemmatyar, M. Taghinejad, H. Taghinejad, A. Krasnok, A. A. Eftekhar, C. Teichrib, S. Deshmukh, M. A. El-Sayed, E. Pop, M. Wuttig, A. Alù, W. Cai, A. Adibi, *Nat. Commun.* **2022**, 13, 1696.
- [25] J. Scoggin, R. Khan, H. Silva, A. Gokirmak, *Appl. Phys. Lett.* **2018**, 112, 193502.
- [26] A. Faraclas, G. Bakan, L. Adnane, F. Dirisaglik, N. E. Williams, A. Gokirmak, H. Silva, *IEEE Trans. Electron Devices* **2014**, 61, 372.
- [27] Y. Zhang, C. Rios, M. Y. Shalaginov, M. Li, A. Majumdar, T. Gu, J. Hu, *Appl. Phys. Lett.* **2021**, 118, 210501.
- [28] S. Abdollahramezani, O. Hemmatyar, H. Taghinejad, A. Krasnok, Y. Kiarashinejad, M. Zandehshahvar, A. Alù, A. Adibi, *Nanophotonics* **2020**, 9, 1189.
- [29] Z. Fang, R. Chen, J. Zheng, A. Majumdar, *IEEE J. Sel. Top. Quantum Electron.* **2021**, 28, 1.

- [30] I. Kim, S. L. Cho, D. H. Im, E. H. Cho, D. H. Kim, G. H. Oh, D. H. Ahn, S. O. Park, S. W. Nam, J. T. Moon, C. H. Chung, in *2010 Symp. on VLSI Technology*, IEEE, Piscataway, NJ **2010**, pp. 203–204.
- [31] D.-H. Kang, S. Y. Kim, S. S. Park, S. H. Eun, J. W. Ma, J. H. Park, I. M. Park, K. S. Park, J. Oh, Z. Wu, J. H. Park, S. W. Jung, H. K. Ahn, Y. Lim, S.-R. Cho, G.-T. Jeong, D.-H. Ahn, S. W. Nam, G. Y. Jin, E. S. Jung, in *2014 14th Annual Non-Volatile Memory Technology Symp. (NVMTS)*, IEEE, **2014**, pp. 1–5.
- [32] K. Aryana, J. T. Gaskins, J. Nag, D. A. Stewart, Z. Bai, S. Mukhopadhyay, J. C. Read, D. H. Olson, E. R. Hoglund, J. M. Howe, A. Giri, M. K. Grobis, P. E. Hopkins, *Nat. Commun.* **2021**, *12*, 774.
- [33] C.-C. Popescu, S. Vitale, C. Roberts, P. Miller, K. Aryana, M. Kang, K. Richardson, H. J. Kim, W. Humphreys, T. Gu, J. Hu, in *Photonic and Phononic Properties of Engineered Nanostructures XIII*, Vol. 12431, SPIE, Bellingham, WA **2023**, pp. 40–48.
- [34] A. Redaelli, A. Pirovano, A. Benvenuti, A. L. Lacaíta, *J. Appl. Phys.* **2008**, *103*, 6.
- [35] A. Sebastian, M. Le Gallo, D. Krebs, *Nat. Commun.* **2014**, *5*, 4314.
- [36] S. G.-C. Carrillo, A. Lugnan, E. Gemo, P. Bienstman, W. H. P. Pernice, H. Bhaskaran, C. D. Wright, *J. Lightwave Technol.* **2021**, *39*, 6392.
- [37] Y. Wang, J. Ning, L. Lu, M. Bosman, R. E. Simpson, *npj Comput. Mater.* **2021**, *7*, 183.
- [38] S. Meyer, Z. Y. Tan, D. N. Chigrin, *Nanophotonics* **2020**, *9*, 675.
- [39] N. Yamada, E. Ohno, K. Nishiuchi, N. Akahira, M. Takao, *J. Appl. Phys.* **1991**, *69*, 2849.
- [40] M. Wuttig, H. Bhaskaran, T. Taubner, *Nat. Photonics* **2017**, *11*, 465.
- [41] M. Salinga, B. Kersting, I. Ronneberger, V. P. Jonnalagadda, X. T. Vu, M. L. Gallo, I. Giannopoulos, O. Cojocar-Mirédin, R. Mazzarello, A. Sebastian, *Nat. Mater.* **2018**, *17*, 681.
- [42] L. Martin-Monier, C. C. Popescu, L. Ranno, B. Mills, S. Geiger, D. Callahan, M. Moebius, J. Hu, *Opt. Mater. Express* **2022**, *12*, 2145.
- [43] J. Orava, A. L. Greer, B. Gholipour, D. Hewak, C. Smith, *Nat. Mater.* **2012**, *11*, 279.
- [44] M. Schumacher, H. Weber, P. Jónvári, Y. Tsuchiya, T. G. A. Youngs, I. Kaban, R. Mazzarello, *Sci. Rep.* **2016**, *6*, 27434.
- [45] M. Salinga, E. Carria, A. Kaldenbach, M. Bornhöft, J. Benke, J. Mayer, M. Wuttig, *Nat. Commun.* **2013**, *4*, 2371.
- [46] X. Li, N. Youngblood, C. Ríos, Z. Cheng, C. D. Wright, W. H. P. Pernice, H. Bhaskaran, *Optica* **2019**, *6*, 1.
- [47] H. Zhang, L. Zhou, L. Lu, J. Xu, N. Wang, H. Hu, B. M. A. Rahman, Z. Zhou, J. Chen, *ACS Photonics* **2019**, *6*, 2205.
- [48] C. Ríos, Q. Du, Y. Zhang, C.-C. Popescu, M. Y. Shalaginov, P. Miller, C. Roberts, M. Kang, K. A. Richardson, T. Gu, S. A. Vitale, J. S. I. Hu, *PhotonIX* **2022**, *3*, 26.
- [49] J. Zheng, Z. Fang, C. Wu, S. Zhu, P. Xu, J. K. Doylend, S. Deshmukh, E. Pop, S. Dunham, M. Li, A. Majumdar, *Adv. Mater.* **2020**, *32*, 2001218.
- [50] S. A. Vitale, P. Miller, P. Robinson, C. Roberts, V. Liberman, Q. Du, Y. Zhang, C.-C. Popescu, M. Y. Shalaginov, M. Kang, K. A. Richardson, T. Gu, C. Ríos, J. Hu, *Adv. Photonics Res.* **2022**, *3*, 2200202.
- [51] J. L. Braun, S. W. King, E. R. Hoglund, M. A. Gharacheh, E. A. Scott, A. Giri, J. A. Tomko, J. T. Gaskins, A. Al-kukhun, G. Bhattarai, M. M. Paquette, G. Chollon, B. Willey, G. A. Antonelli, D. W. Gidley, J. Hwang, J. M. Howe, P. E. Hopkins, *Phys. Rev. Mater.* **2021**, *5*, 035604.
- [52] A. Cappella, J.-L. Battaglia, V. Schick, A. Kusiak, A. Lamperti, C. Wiemer, B. Hay, *Adv. Eng. Mater.* **2013**, *15*, 1046.
- [53] K. Aryana, Y. Zhang, J. A. Tomko, M. S. B. Hoque, E. R. Hoglund, D. H. Olson, J. Nag, J. C. Read, C. Ríos, J. Hu, P. E. Hopkins, *Nat. Commun.* **2021**, *12*, 7187.
- [54] J. Zhao, J. Hui, Z. Ye, T. Lai, M. Y. Efremov, H. Wang, L. H. Allen, *Adv. Mater. Interfaces* **2022**, *9*, 2200429.
- [55] K. T. Regner, D. P. Sellan, Z. Su, C. H. Amon, A. J. H. McGaughey, J. A. Malen, *Nat. Commun.* **2013**, *4*, 1640.
- [56] Y. Zhang, J. Li, J. Chou, Z. Fang, A. Yadav, H. Lin, Q. Du, J. Michon, Z. Han, Y. Huang, H. Zheng, T. Gu, V. Liberman, K. Richardson, J. Hu, in *CLEO: Science and Innovations*, Optica Publishing Group, Washington, DC **2017**, pp. JTh5C–4.
- [57] Y. Zhang, J. B. Chou, J. Li, H. Li, Q. Du, A. Yadav, S. Zhou, M. Y. Shalaginov, Z. Fang, H. Zhong, C. Roberts, P. Robinson, B. Bohlin, C. Ríos, H. Lin, M. Kang, T. Gu, J. Warner, V. Liberman, K. Richardson, J. Hu, *Nat. Commun.* **2019**, *10*, 4279.
- [58] A. K. Varshneya, *Fundamentals of Inorganic Glasses*, Elsevier, Amsterdam **2013**.
- [59] W. W. Koelmans, A. Sebastian, V. P. Jonnalagadda, D. Krebs, L. Dellmann, E. Eleftheriou, *Nat. Commun.* **2015**, *6*, 8181.
- [60] C. Ríos, M. Stegmaier, Z. Cheng, N. Youngblood, C. D. Wright, W. H. P. Pernice, H. Bhaskaran, *Opt. Mater. Express* **2018**, *8*, 2455.
- [61] S. Senkader, C. Wright, *J. Appl. Phys.* **2004**, *95*, 504.
- [62] G. K. Johnson, G. Papatheodorou, C. E. Johnson, *J. Chem. Thermodyn.* **1981**, *13*, 745.
- [63] A. Pashinkin, A. Malkova, M. Mikhailova, *Russ. J. Phys. Chem. A* **2008**, *82*, 1035.
- [64] H. Zhang, L. Zhou, J. Xu, N. Wang, H. Hu, L. Lu, B. M. A. Rahman, J. Chen, *Sci. Bull.* **2019**, *64*, 782.
- [65] J. Zheng, S. Zhu, P. Xu, S. Dunham, A. Majumdar, *ACS Appl. Mater. Interfaces* **2020**, *12*, 21827.
- [66] O. Abed, L. Yousefi, *Opt. Express* **2020**, *28*, 33876.
- [67] H. Zhang, X. Yang, L. Lu, J. Chen, B. M. A. Rahman, L. Zhou, *Opt. Express* **2021**, *29*, 3503.
- [68] Y. Zhang, C. Fowler, J. Liang, B. Azhar, M. Y. Shalaginov, S. Deckoff-Jones, S. An, J. B. Chou, C. M. Roberts, V. Liberman, M. Kang, C. Ríos, K. A. Richardson, C. Rivero-Baleine, T. Gu, H. Zhang, J. Hu, *Nat. Nanotechnol.* **2021**, *16*, 661.
- [69] C. Ríos, Y. Zhang, M. Y. Shalaginov, S. Deckoff-Jones, H. Wang, S. An, H. Zhang, M. Kang, K. A. Richardson, C. Roberts, J. B. Chou, V. Liberman, S. A. Vitale, J. Kong, T. Gu, J. Hu, *Adv. Photonics Res.* **2021**, *2*, 2000034.
- [70] D. Lawson, D. W. Hewak, O. L. Muskens, I. Zeimpekis, *J. Opt.* **2022**, *24*, 064013.
- [71] C. Zhang, M. Wei, J. Zheng, S. Liu, H. Cao, Y. Huang, Y. Tan, M. Zhang, Y. Xie, Z. Yu, J. Li, H. Ye, L. Li, H. Lin, H. Li, Y. Shi, L. Liu, D. Dai, *Adv. Opt. Mater.* **2023**, 2202748.
- [72] P. Pustkova, D. Švadlák, J. Šánělová, J. Málek, *Thermochim. Acta* **2006**, *445*, 116.
- [73] E. Černošková, R. Todorov, Z. Černošek, J. Holubová, L. Beneš, *J. Therm. Anal. Calorim.* **2014**, *118*, 105.
- [74] J. Kalb, M. Wuttig, F. Spaepen, *Int. J. Mater. Res.* **2007**, *22*, 748.
- [75] Y. Tae Kim, S.-I. Kim, *Appl. Phys. Lett.* **2013**, *103*, 121906.
- [76] R. Endo, S. Maeda, Y. Jinnai, R. Lan, M. Kuwahara, Y. Kobayashi, M. Susa, *Jpn. J. Appl. Phys.* **2010**, *49*, 065802.
- [77] T. Siegrist, P. Jost, H. Volker, M. Woda, P. Merkelbach, C. Schlockermann, M. Wuttig, *Nat. Mater.* **2011**, *10*, 202.
- [78] L. Crespi, A. Ghetti, M. Boniardi, A. L. Lacaíta, *IEEE Electron Device Lett.* **2014**, *35*, 747.
- [79] D. Baratella, D. Dragoni, M. Bernasconi, *Phys. Status Solidi RRL* **2022**, *16*, 2100470.